Influence of temperature on the aging behavior of 18650-type lithium ion cells: A comprehensive approach combining electrochemical characterization and *post-mortem* analysis

Alex Friesen [a, b], Xaver Mönnighoff [a, b], Markus Börner [a, b], Jan Haetge [a], Falko M. Schappacher [a, *], Martin Winter [a, b, c, **]

[a] MEET Battery Research Center, University of Muenster, Corrensstraße 46, 48149 Muenster, Germany
[b] Institute of Physical Chemistry, University of Muenster, Corrensstraße 28/30, 48149 Muenster, Germany
[c] Helmholtz-Institute Muenster, IEK 12, Forschungszentrum Juelich GmbH, Corrensstraße 46, 48149 Muenster, Germany

HIGHLIGHTS

- FEC influence on aging and degradation of PC/EC/DMC based electrolyte.
- Complex interaction of electrolyte and electrode in dependency of the temperature.
- Exfoliation of graphite as a result of solvent co-intercalation at 20 °C.
- Exfoliation results into massive electrolyte decomposition and a thick SEI layer.
- Stable and effective SEI at anode enables good electrochemical performance at 45 °C.

GRAPHICAL ABSTRACT
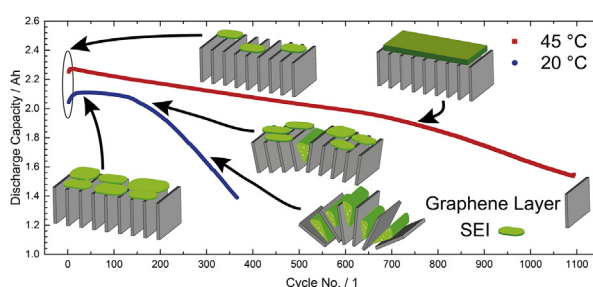
ARTICLE INFO

ABSTRACT

The understanding of the aging behavior of lithium ion batteries in automotive and energy storage applications is essential for the acceptance of the technology. Therefore, aging experiments were conducted on commercial 18650-type state-of-the-art cells to determine the influence of the temperature during electrochemical cycling on the aging behavior of the different cell components. The cells, based on $Li(Ni_{0.5}Co_{0.2}Mn_{0.3})O_2$ (NCM532)/graphite, were aged at 20 °C and 45 °C to different states of health. The electrochemical performance of the investigated cells shows remarkable differences depending on the cycling temperature. At contrast to the expected behavior, the cells cycled at 45 °C show a better electrochemical performance over lifetime than the cells cycled at 20 °C. Comprehensive *post-mortem* analyses revealed the main aging mechanisms, showing a complex interaction between electrodes and electrolyte. The main aging mechanisms of the cells cycled at 45 °C differ strongly at contrast to cells cycled at 20 °C. A strong correlation between the formed SEI, the electrolyte composition and the electrochemical performance over lifetime was observed.

 * Corresponding author. MEET Battery Research Center, University of Muenster, Corrensstraße 46, 48149 Muenster, Germany.
 ** Corresponding author. Helmholtz-Institute Muenster, IEK 12, Forschungszentrum Juelich GmbH, Corrensstraße 46, 48149 Muenster, Germany.
  E-mail addresses: falko.schappacher@uni-muenster.de (F.M. Schappacher), martin.winter@uni-muenster.de, m.winter@fz-juelich.de (M. Winter).

1. Introduction

Lithium ion batteries (LIBs) offer a high energy density, high power density and high charge/discharge Coulombic and energy efficiencies [1–3]. They are considered as the key technology for portable electronic devices. In the emerging field of automotive applications LIBs are considered as one major energy source to power electric vehicles. The utilization of LIBs in hybrid electric vehicles (HEV), plug-in hybrid electric vehicles (PHEV) and electric vehicles (EVs) is strongly increasing. Furthermore, the upgrade from 12 V to 48 V vehicle electrical systems in internal combustion engine (ICE) powered cars is becoming more popular. Moreover, energy storage systems on a LIB basis are regarded as one possible near-term solution to deal with the fluctuating power generation of renewable energy sources. At contrast to portable electronic devices, for the automotive and energy storage application a much longer-term operation is essential for consumer satisfaction. The goals, as set by the USABC for 2018, are 15 years of calendar life, 1000 cycles for EVs and 5000 cycles for PHEVs before the end-of-life (EOL) of the battery is reached. EOL is defined as a state of health (SOH) of 70–80% in comparison to the discharge capacity of the fresh cell [4,5]. To ensure a sufficient lifetime of the cells for the respective application, it is essential to understand the correlation between the influence of the operation parameters on the electrochemical performance over lifetime and the related aging mechanisms.

Aging of LIBs is a topic of various, very often inter-dependent chemical and physical changes of the cell materials resulting in capacity fading, resistance increase, and thus loss in power and energy densities [6]. Moreover, different aging processes originate from a number of various degradation mechanisms and their interactions. Most studies focus on aging of individual parts of the cell, such as the electrolyte decomposition [7,8], cathode decomposition [9,10], electrolyte and anode interactions [11,12], electrolyte and cathode interactions [13–15], solid electrolyte interphase growth [16,17], graphite aging [18,19], cathode electrolyte interphase growth [20], lithium metal deposition [21,22] and many more [6,23]. Overall, there is still a lack of extensive studies which determine aging of all components and their interactions at different aging conditions (e.g. cycling temperature).

In this work, the influence of aging at different temperatures is studied on commercial 18650-type lithium ion cells, based on Li(Ni$_{0.5}$Co$_{0.2}$Mn$_{0.3}$)O$_2$/graphite. The cells were cycled at 20 °C and at 45 °C in order to investigate the temperature dependent aging behavior.

To study the electrochemical performance and the thermal impact of the aging effects, the cells were cycled to different state of healths (SOHs). Combined electrochemical and *post-mortem* analysis were performed to investigate the influence of the temperature in detail. The focus of this study is to reveal the major aging mechanisms of the main components, including the anode, cathode and electrolyte. This work provides information about the different stages of aging and the key parameters of the aging mechanisms affecting the cell lifetime. In parallel, a second study will be published by Börner et al. revealing the correlation of aging and the cell behavior under thermal abuse of the presented cells.

2. Experimental

2.1. Cell choice

The cell under investigation is a commercially available 18650-type lithium ion cell. The cell chemistry is based on a Li(Ni$_{0.5}$Co$_{0.2}$Mn$_{0.3}$)O$_2$ (NCM) cathode and a graphitic anode. The electrolyte of a fresh cell consists of LiPF$_6$ as electrolyte salt, dimethyl carbonate (DMC), ethylene carbonate (EC) and propylene carbonate (PC) as organic solvents. Fluoroethylene carbonate (FEC), propane-1,3-sultone (PS) and succinonitrile (SN) were used as electrolyte additives to improve the cell performance. The separator consists of a polyethylene (PE) based one layer foil. With a nominal discharge capacity of 2.2 Ah and a maximum discharge current rate of 2C (4.4 A) the cell can be classified as a middle power cell, typically used in applications with the demand of balanced power to capacity ratio, e.g. pedelecs and notebooks. The cell specifications are summarized in Table S1.

2.2. Cell aging and electrochemical analysis

Cycle aging experiments were performed with a Maccor Series 4000 Battery Tester (Maccor, Inc., USA) in a Binder KB 400 climate test chamber (BINDER GmbH, Germany) at constant chamber temperatures of 20 °C and 45 °C. The cycling protocol consists of a constant current/constant voltage (CC/CV) charge followed by a CC discharge. The upper and lower cut-off voltages were set to 4.2 V and 2.75 V respectively in accordance with the MSDS (see supporting information Table S1). The CC step was performed with a C-rate of 1 C (2.2 A) and the CV step until the current falls below C/20 (0.11 A). The end of life was defined as a SOH less than or equal to 90%, 80% and 70%, respectively. In the beginning and after every 50th cycle, the direct current inner resistance (DCIR) was determined with a protocol defined by the VDA (German Association of the Automotive Industry). According to the protocol the discharge resistance is calculated from a 18 s constant current discharge pulse with a high C-rate and the charge resistance is calculated from a charge pulse. The inner resistance in this work was determined at a state of charge (SOC) of 50% with a maximum discharge current of 6 A. The maximum C-rate was defined in a previous test analyzing the behavior of the cells at different C-rates. The voltage response of the cell is shown in Fig. S1. Additional electrochemical impedance spectroscopy (EIS) measurements were performed at 20 °C in potentiostatic mode with a sinusoidal amplitude of 10 mV between 10 kHz and 100 mHz. Electrochemical impedance measurements were performed using a Solartron (AMETEK, Inc., USA) device which consists of a 1287A potentiostat and a 1260A impedance gain phase analyzer. The impedance spectra were recorded at 50% SOC.

2.3. Sample preparation

Before cell opening, an extended discharge step was carried out, composed of a CC/CV protocol (limit < 0.05C) to ensure a minimized energy content and reactivity of the cell during disassembly. The discharged cells were subsequently opened in a glove box (M. Braun Inertgas-Systeme GmbH, Germany) under argon atmosphere (O$_2$, H$_2$O < 0.1 ppm) by slicing the two ends of the metal shell with an cutting tool (build from the workshop), similar to the self-made cutter from Aurbach et al. [24], to prevent short-circuits or any other destructive side-reactions during cell opening. The case was carefully removed to unwind the jelly roll. The individual parts of the cell (outer separator, anode, inner separator, and cathode) were separated. The extracted samples were washed twice with 800 μL dimethyl carbonate (DMC by Sigma-Aldrich, anhydrous, ≥ 99%, USA) from both sides to remove residues of the conductive salt and other electrolyte components. Afterwards the samples were dried in the glove box.

2.4. Structure, morphology and composition of electrodes

The electrode morphology was investigated by scanning electron microscopy (SEM). SEM images were obtained using a Carl

Zeiss AURIGA CrossBeam workstation (Carl Zeiss SMT AG, Germany) with an acceleration voltage of 3 kV at a working distance of 2 mm under a vacuum of 10^{-6} bar. Energy dispersive X-ray spectroscopy (EDX) was used at 20 kV and 5 mm working distance to analyze the elemental composition of particles and the surfaces of interest using an integrated EDX-detector INCA x-max 80 mm^2 (Oxford Instruments, UK). A focused ion beam (FIB) technique was applied to generate a cross-section of the electrode surface by milling with high-energy gallium ions. FIB was used at 5 mm working distance, a two steps milling process was performed using a milling current of 20 μA and 500 pA, respectively.

2.5. Determination of the electrolyte composition

2.5.1. Sample preparation and extraction procedure

The jelly role as well as the stack were removed of the shell, uncoiled and plugged, as dense as possible, into the vessel of the extraction equipment according to Grützke et al. [8]. After connecting the extraction vessel to the CO_2 supply and adjusting pressure and temperature in the chamber to supercritical conditions (40 °C, 200 bar), the extraction begun with a static (non-flow-through) equilibration step which was hold for 30 min, followed by 5 min of CO_2 flow-through with addition of the co-solvent (ACN, 0.5 mL/min) and subsequent 5 min equilibration. After two repetitions, two runs were performed without co-solvent. Via a heated outlet valve (55 °C) the CO_2 stream was transferred into a series of two cryogenic traps of aluminum (−78 °C). The electrolyte and co-solvent were frozen out and the yield was determined by weight.

2.5.2. Analytical equipment

Supercritical Fluid extraction (SFE). All extraction experiments were done in a dry room (dew point: −65 °C; H_2O < 5.4 ppm). An Applied Separations Spe-ed SFE System purchased from ERC, which is equipped with a Knauer Platin Blue UHPLC pump for the addition of the co-solvent, was used for the extraction experiments. The extraction chamber (50 mL) and all gas lines consist of stainless steel. At the beginning of each extraction experiment, the device was investigated for gas leaks. Furthermore, the CO_2 flow was adjusted to (8 ± 1) L/min.

Gas chromatography-mass spectrometry (GC-MS). A Shimadzu GCMS-QP2010 Ultra GC-MS equipped with an AOC-5000 Plus autosampler and a Supelco SLB-5ms column (30 m × 0.25 mm × 0.25 μm) was used. The GCMS Solution software (GCMS Real Time Analysis and GCMS Postrun Analysis) was used for setup control and data analysis. DMC, EC, PC, VC, FEC, SN and PS were identified by the NIST11 library. Furthermore, these substances and DMDOHC were identified by retention time of the pure substances.

The samples were diluted in a ratio of 1:100 in DCM and 1 μL was injected at 250 °C with a split ratio of 1:20. The system was run with a column flow of 1.16 mL/min Helium, a purge flow of 3 mL and the following column oven program: starting at 40 °C held for 1 min, the temperature was increased by a rate of 3 °C/min up to 60 °C and further by a rate of 30 °C/min up to 210 °C and held for 1 min. The MS was operated in the electron impact (EI) ionization mode with a filament voltage of 70 V and a detector voltage which was chosen relative to tuning results. As working range 10−300 *m/z* was chosen with an event time of 0.1 s, an ion source temperature of 200 °C and an interface temperature of 250 °C.

3. Results and discussion

3.1. Cyclic aging

The cells were cycled to an SOH of 90%, 80% and 70%,

respectively, to reproduce the entire progression of the aging processes at 20 °C and at 45 °C during cycling. The electrochemical cycling data for two selected cells aged until a 70% SOH at 20 °C and at 45 °C are shown in Fig. 1 as they represent the most severe aging in this work. Additional cycling data are presented in Fig. S2. Opposite to expectation, the cells cycled at 45 °C show a better discharge capacity and capacity retention in comparison to the cell cycled at 20 °C (Fig. 1a). This cell accomplished approximately 1100 cycles until the EOL criteria of 70% SOH was reached. The discharge capacity is fading in a nearly linear manner. At contrast, the cell cycled at 20 °C shows small capacity fading in the first 100 cycles, followed by an accelerated fading. The SOH of 70% is reached already at approximately 350 cycles. In addition, both cells show an increase in capacity in the first cycles. As shown in Fig. 1b) the Coulombic efficiency (CE) in this cycle is above 1 (>100%). Hence the charge capacity is smaller compared to the discharge capacity of the same cycle. A reason might be unused capacity in previous cycles, which has been activated. Prolonged cycling causes the CE to drop below 1 for both cells. The cells cycled at 20 °C have a high and stable CE in the first 100 cycles, which represents a minor loss of active lithium during charge and discharge reactions. With further aging the CE decreases and indicates an increasing loss of active lithium. The change of the CE course suggests a severe degradation of one of the battery components for the cell cycled at 20 °C. Cycling at higher temperatures (45 °C) shows a lower CE at the beginning compared to cycling at 20 °C. The lower CE may result from electrolyte decomposition, contact loss of active material, binder degradation and/or lithium reduction on anode surface [6]. A nearly constant CE below 1 at 45 °C indicates a continuous side reaction in the cell. A lower CE compared to the cell cycled at 20 °C (first 100 cycles) suggests a side reaction enhanced by higher temperatures such as electrolyte decomposition, solid electrolyte interphase (SEI) [16,25] and cathode electrolyte interphase (CEI) [26] growth and/or binder degradation [27].

Each 50th cycle, the direct current internal resistance (DCIR) was determined by the VDA method [28]. The results are shown in Fig. 1c). Both cells exhibit a drop in resistance in the first cycles. Cycling at 45 °C shows a linear increase of the resistance over the lifetime. The cell cycled at 20 °C shows a linear increase and after 150 cycles an accelerated increase of resistance. Both resistance results correlate with the discharge capacity. A higher resistance decreases the amount of intercalated and de-intercalated lithium in the electrodes by over-potentials. The lower resistance of the cell cycled at 45 °C is assumed to result from improved ionic conductivity and enhanced mobility of Li^+ in the electrodes as well as better charge-transfer at the interface at higher temperatures. Additionally, the discharge mean voltage of the cycled cells is illustrated in Fig. 1d). For the first cycles (cycle range 1−20) the cells present a voltage increase. Cells at higher temperatures show a higher discharge mean voltage, due to better kinetics and lower over-potentials. After the first cycles the 20 °C cells directly show a strong discharge mean voltage fading, indicating an early onset of degradation mechanisms. After 200 cycles, voltage fading increases even more. Voltage fading of the cell cycled at 45 °C is increasing slowly, indicating no abrupt changes in the aging behavior during long-term cycling.

The cycling results show a strong dependency of the cycling temperature. It can be concluded that different aging mechanisms occur in the cells affecting the electrochemical performance. The cells cycled at 45 °C show a stable cycling performance, indicating a homogeneous aging mechanisms that do not change significantly over the lifetime. At contrast, the cells cycled at 20 °C show a different aging behavior. The cycling performance changes drastically after approximately 100−150 cycles, indicating the onset of additional or accelerated degradation mechanisms, leading to
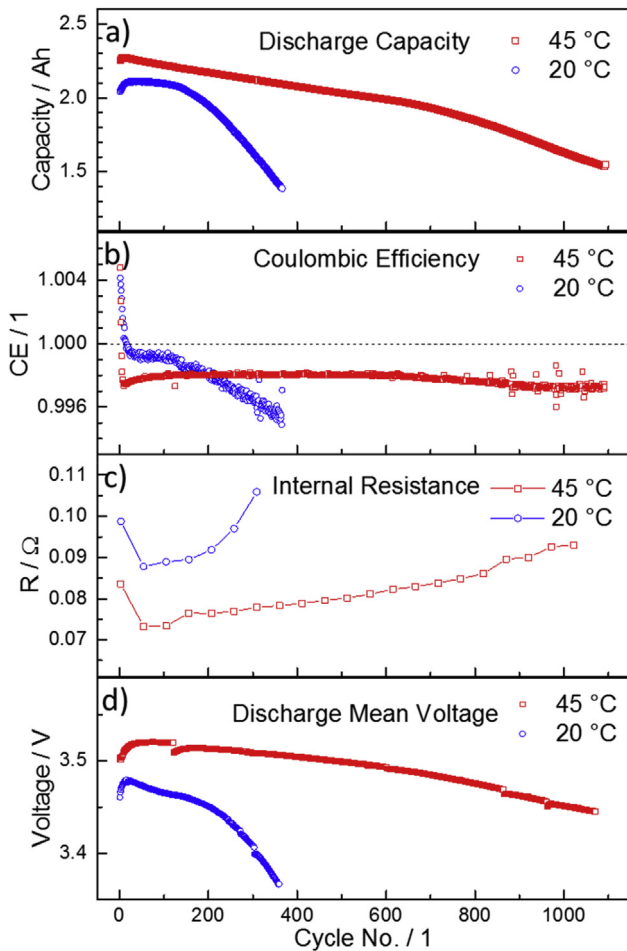
Fig. 1. Cells aged at 20 °C and at 45 °C until an SOH of 70%, showing discharge capacity evolution (a), Coulombic efficiency (b), determined direct current internal resistance (DCIR) at 50% SOC (VDA protocol) (c) and the discharge mean voltage (d) in dependency of the cycle number.

increased capacity fading, voltage fading and DCIR increase.

To further investigate the aging mechanisms and the capacity increase in the initial cycles, EIS measurements were performed on cells cycled at 20 °C. The measurements were performed at 50% SOC to allow a comparison with the DCIR measurement obtained by the VDA method [28]. By fitting the electrochemical impedance spectra the R_0 and R_1 parts were extracted. The ohmic resistance R_0 is attributed to the Li$^+$ transport through the electrolyte, contact losses and the electronic conductivity of electrodes and current collector [29]. The changes over the lifetime of the cell can be attributed to the conductivity changes of the electrolyte, as the other impacts are unlikely to change. The resistance R_1 represents the Li$^+$ migration thought the passivating layers and the charge transfer resistances [25,30].

In the first cycles (section I. in Fig. 2) a slight increase of R_0 and a comparably large decrease of R_1 is visible. This Indicates electrolyte decomposition and a change of the SEI/charge transfer characteristics. As the electrolyte is predominantly reduced on the anode surface by forming the SEI, the results suggests a transformation to a more effective SEI with a lower Li$^+$ migration and charge transfer resistance than after formation by the cell manufacturer, indicating an ineffective formation procedure. In total the cell resistance is decreasing, whereas the discharge capacity increases. The decrease of the internal resistance in the cells cycled at 45 °C in the first cycles is assumed to result from similar cell resistance changes as in

the 20 °C cells (Fig. 1c). With further cycling (section II. in Fig. 2) a slight increase of R_0 and a constant R_1 is observable, followed by a strong increase of both resistances (section III. in Fig. 2). For a deeper understanding of these performance changes, comprehensive *post-mortem* analyses have been performed.

3.2. Visual analysis of opened cells

After removing the cell case, the jelly rolls were unrolled. A comparison of fresh and aged electrodes is shown in Fig. 3.

The fresh cathode shows losses of the cathode laminate and exposes a blank aluminum current collector (Fig. 3a). Partly, the cathode laminate sticks to the separator or is broken and falls apart. The inner layer of the electrode (increasing winding angle) showing more brittle characteristics, as the material falls apart by unrolling it. With aging, this effect is even more pronounced as shown in Fig. 3c and e for cathodes aged at 20 °C and at 45 °C, resulting in a mostly blank aluminum current collector foil. The cathode coating of all aged cells (90%—70% SOH, at 20 °C and 45 °C) was very brittle. Remaining cathode active material was only present in the beginning of the coil, indicating a less profound aging in this region of the cell, which might relate with the smaller winding angle of the coil at this position, thus, leading to less mechanical stress in the beginning of the coil. Polyvinylidene difluoride (PVdF) is used as a binder for the cathode material in this cells. It was reported that PVdF is easily weakened at high temperatures (60 °C), losing mechanical strength [31]. Since the cathode aged at 20 °C shows similar results, a similar degradation mechanism is likely.

The fresh anode (Fig. 3b) shows a homogenous coating of the anode laminate on the Cu current collector. Similar to the cathodes, cycling the cell at 45 °C results in a nearly blank copper current collector (Fig. 3d) with some residues of the anode in the beginning. The anode aged at 20 °C seems to be in a good condition, as shown in Fig. 3f). The Cu current collector is visible partially in small spots. The reason for the difference in the degradation of cathode and anode might originate from the binder used in anode and cathode.
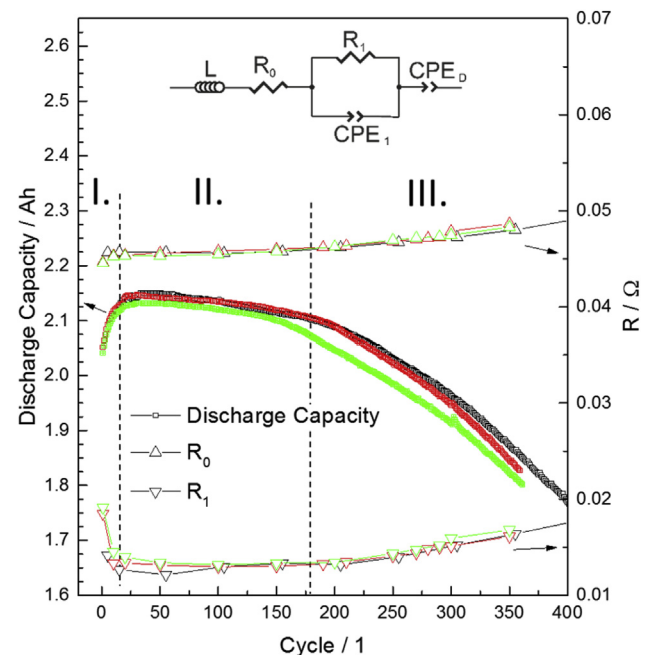

Fig. 2. Evolution of electrolyte resistance and charge transfer resistance in dependency of the cycle number for 3 cells cycled at 20 °C. The equivalent circuit presented in this figure has been used to extract the resistance values from the EIS results. I., II. and III. refer to different aging sections discussed in the text.

A mixed sodium carboxymethyl cellulose (Na-CMC) and styrene butadiene rubber (SBR) binder in the anode possesses a similar bonding ability, but a higher flexibility compared to poly (vinylidene fluoride) (PVdF) [32]. Graphite shows a volume change during cycling [33,34], a higher mechanical degradation of the binder can be assumed at 45 °C by cycling nearly three times longer compared to 20 °C at a similar SOH. Further causes such as electrochemical degradation might have an additional impact.

3.3. Morphology of fresh and aged electrodes

SEM images of fresh and aged electrodes were used to characterize the morphological change. A comparison between fresh and aged cathodes is shown in Fig. 4. All samples were taken from parts of the electrodes where the cathode laminate is still existent. The fresh cathode consists of spherical secondary particles of Li(Ni$_{0.5}$Co$_{0.2}$Mn$_{0.3}$)O$_2$ surrounded by a conductive agent and PVdF binder. The particles on the surface of the fresh electrodes show a flattened surface which results from calendering of the electrode (see Fig. 4a and b). A loss of material is visible in the images of the aged cathodes at 20 °C and at 45 °C, revealing the inner (lower) parts of the coating layer. The flattened surface resulting from calendering is not present, suggesting a loss of the outer (upper) cathode layer. The aluminium current collector is partially visible (red circles, Fig. 4c, e). Considering the cross-section of the cathode layer (Fig. S4), a loss of approximately 50–70% of the cathode material can be estimated. The capacity fading is not necessarily resulting from mechanical degradation of the binder and the consequential particle isolation and delamination. The cell volume is fixed (18650-type) with a rigid cylindrical stainless steel case holding the cell components tight. Upon opening, this cell compression is loosened and the cathode laminate can fall apart, as shown in section 3.3. Independent from binder aging, the cell shows a discharge capacity of approximately 80% compared to the fresh cells.

SEM images of the fresh and aged anodes are shown in Fig. 5. The fresh anode shows potato-shaped graphite particles. The higher magnification reveals (Fig. 5b) deposits on the surface of the graphite particles (e.g. red circle), which can be attributed to the SEI. The surface film is uneven and inhomogeneous. Thus, the increase in electrolyte resistance and decrease in charge transfer resistance in the first cycles can be explained with a fast and insufficient formation of the cells by the OEM, as described in section 3.1.

The cells cycled at 20 °C show three different aging sections (Fig. 2). To identify the main aging mechanisms, anode samples at the end of the second and third section were analyzed. Fig. 5c) shows the anode after 100 cycles. The initial morphology of the electrode is still visible. It seems, a new surface layer covers the graphite particles. At higher magnifications (Fig. 5d) the onset of

the delamination of the graphite particles can be identified. This phenomenon is known as exfoliation which is typically expected to take place within the initial cycles [33]. Since the investigated sample is at an intermediate state between section II. and III., this observation can be assigned to the beginning of the exfoliation phenomenon. This indicates an inhibited exfoliation in the first 100 cycles due to the SEI protection. By further cycling a thick layer arise on the anode, as visible in Fig. 5e and f. The left-central area in Fig. 5 e) shows a partial removal of the layer, revealing changes of the graphite surface underneath the layer. The cracks in the new layer may result from the sample preparation. Additionally the layer shows a high static electric charge during SEM investigations, indicating a poor electric conductivity of the new surface layer.

Exfoliation, i.e. shedding of graphene layers and graphene layer packages of graphite is caused, as proposed in Refs. [35–37], by solvent molecule co-intercalation along with the lithium ions in the interlayer gaps of graphite. The co-intercalated solvent molecules decompose inside the graphite structure leading to massive ethylene and propylene gas evolution [34], and subsequent disintegration/exfoliation of the graphite structure. To further investigate the exfoliation phenomenon a cross-section of the anode layer close to the surface was prepared by a FIB milling process, as shown in Fig. 6. The thickness of the layer is approximately 20 μm at the examined position. A higher magnification shows the presence of a homogeneous "deposition" on the anode surface in the middle of the layer cross cut (Fig. 6b). An analysis with the energy dispersive x-ray (EDX) spectroscopy did not reveal clear results (see Fig. S6). Thus, the deposited material might be below the detection limits of the EDX, which is for instance the case for metallic Li. As the internal resistance increases with cycling, overpotentials can push the potential of the graphite anode below 0 V vs Li/Li$^+$ resulting in lithium metal deposition on the surface of graphite. This might be an explanation for the bright spot. Beside, a network of lines becomes visible with further magnification in Fig. 6c). The lines can be attributed to graphitic fragments while an intact graphite structure is observed in the lower part of the cross-section. The upper part shows a huge expansion and scattering of the graphene layer and indicates an advanced state of exfoliation. The separation of both parts is visible in the EDX mapping in Fig. 6d). The carbon and oxygen signal show a separation between the graphite particle (missing oxygen signal) and the exfoliation layer (pronounced carbon and oxygen signal). The oxygen signal can be contributed to electrolyte decomposition products containing oxygen. In between the graphene layer packages electrolyte decomposition products are likely. Fresh and charged electrodes surface exposed to the electrolyte results in the formation of a new SEI by reduction of electrolyte [38]. As a side reaction gaseous electrolyte decomposition products are generated. This may explain the overall porous structure of the layer. The marked ellipse in Fig. 6c) shows a closed gap between two graphene layers, including electrolyte and a gas
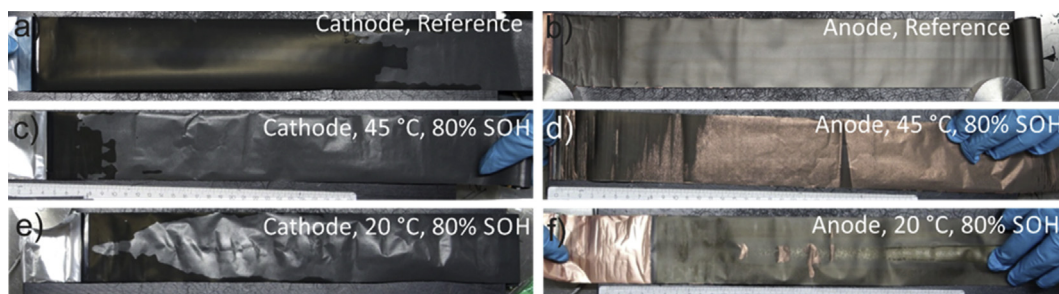

Fig. 3. Unrolled electrodes of fresh and aged cells, showing a fresh cathode (a), a fresh anode (b), an at 45 °C aged (80% SOH) cathode and anode (c,d) and an at 20 °C aged cathode and anode (e,f) after opening in the glovebox.
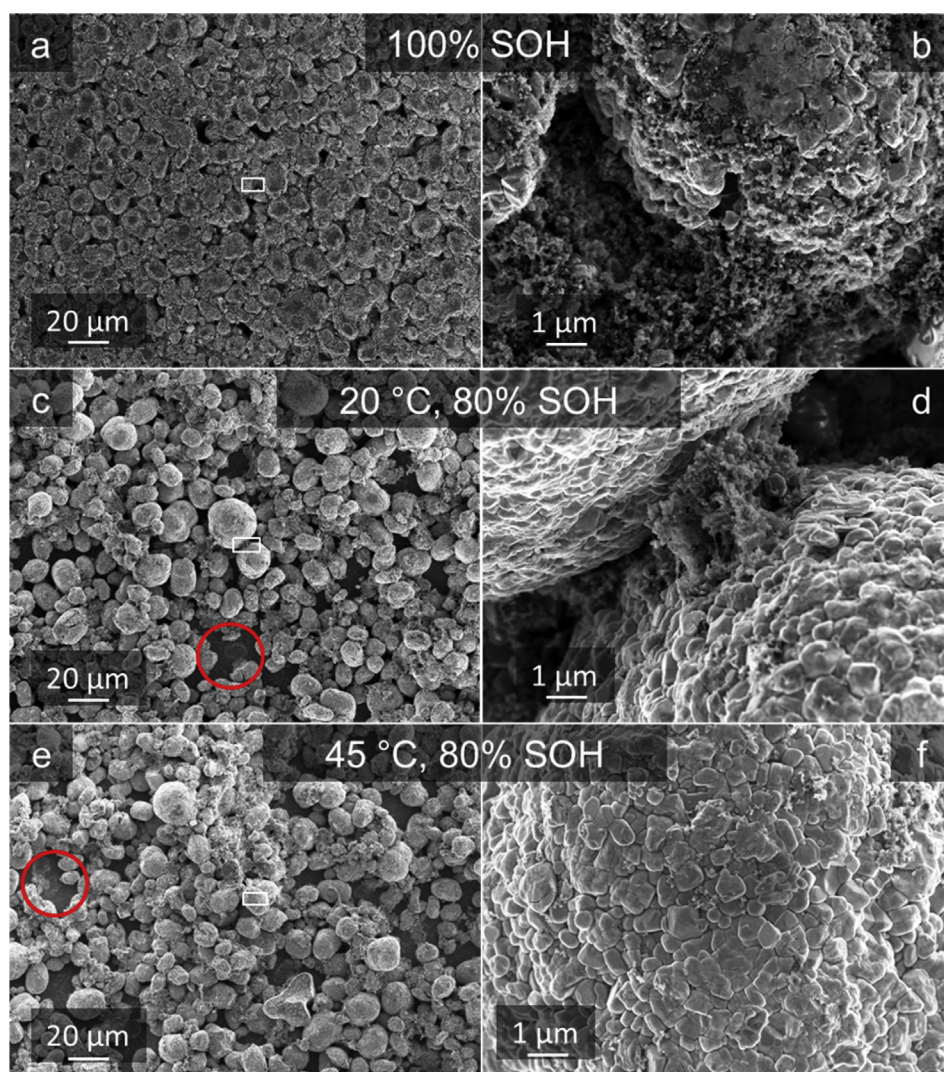
Fig. 4. SEM images with two different magnifications of the fresh cathode (a,b), the cathode cycled at 20 °C (c,d) and the cathode cycled at 45 °C (e,f).

pore in between. This supports the model proposed in Refs. [35–37] in which such cavities can be formed by co-intercalation of solvent molecules and subsequent gas formation. Independent of the exfoliation mechanisms the electrolyte is the main driving force for the degradation process.

Aging at 45 °C changes the surface slightly, as shown in Fig. 5g). The graphite particles are still visible. At some electrode tape spots, fractions of the electrode coating material are missing, which correlates well with the visual analysis of the electrode after opening (section 3.3), indicating a loss in mechanical stability, resulting from binder degradation. This reconfirms, that the binder degradation does not necessarily lead to capacity fading, as long as the cell components are under compression. The higher magnification reveals a further aging mechanism. Compared to the fresh anode, a thicker but more homogenously distributed SEI is formed on the graphite surface. As the cells cycled at 45 °C show a much better cycling behavior in comparison to the cells cycled at 20 °C, it can be concluded that a more effective SEI is formed at higher temperatures.

3.4. Electrolyte aging

Electrolyte samples extracted from fresh and aged cells were analyzed by GC-MS (Fig. 7). The electrolyte of the fresh cell consists of dimethyl carbonate (DMC), ethylene carbonate (EC) and pro-pylene carbonate (PC) as solvents [39], whereas fluoroethylene carbonate (FEC) [40] and succinonitrile (SN) [41] were identified as electrolyte additives in significant amounts. Furthermore, traces of vinylene carbonate (VC) [42] and 1,3-propane sultone (PS) [43] were detected in the electrolyte. VC might origin from the reduction of FEC which reacts to hydrogen fluoride (HF) and VC [44].

The cell aged at 45 °C shows traces of FEC in the electrolyte after more than 1000 cycles. FEC is a film-forming additive, which improves cycling stability and CE at various conditions [44–47] due to an effective SEI consisting of large amounts of lithium fluoride (LiF) and polymerization products [47–49]. Less effective, organic SEI components are mostly suppressed by inorganic SEI components with the addition of FEC [50].

In the cells cycled at 45 °C, the amount of VC and PS was below the limit of detection. VC polymerizes on the graphite surface, which show a better cycling performance, especially at elevated temperatures [51]. Zou et al. [52] showed that the reduction of PS leads to the formation of an effective SEI on the graphite surface. Furthermore, PS showed these advantages, both for cycling [43] and storage [53] at higher temperatures. The improvement was attributed to an SEI with an enhanced ionic conductivity [43]. Therefore, the combination of VC and PS results in an increased
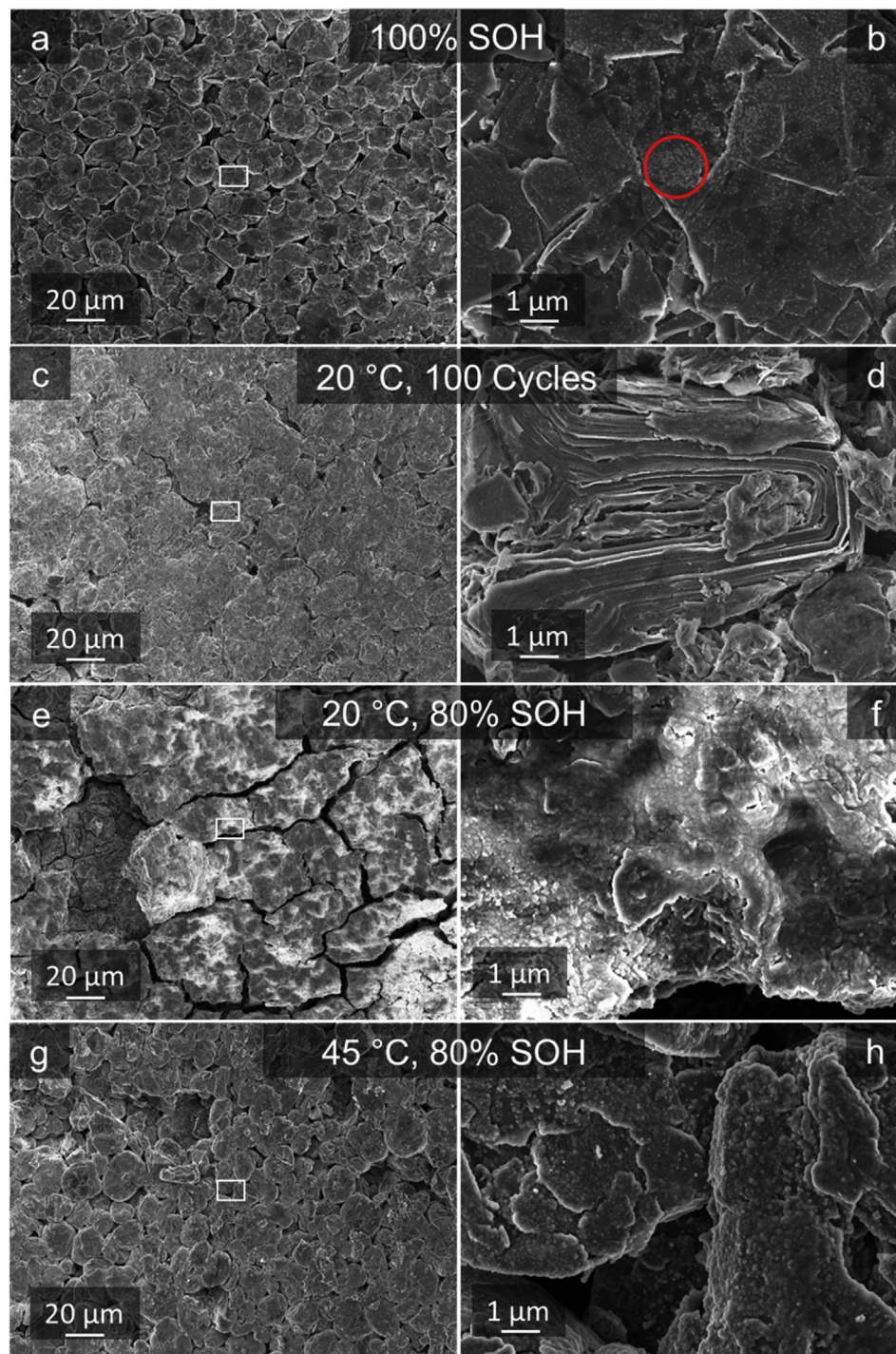
Fig. 5. SEM images of anode surfaces at two different magnifications for a fresh anode (a,b), anode cycled at 20 °C for 100 cycles (c,d), anode cycled at 20 °C to a SOH of 80% (e,f) and anode cycled at 45 °C to a SOH of 80% (g,h).

stability and ion-conductivity compared to an SEI formed without these additives [43]. Both effects are explained with a decreased fraction of lithium ethylenedicarbonate (LEDC) and lithium alkyl carbonates (Li_2CO_3) and the formation of poly (VC) and RSO_3Li in the SEI [43]. As shown by Herstedt et al. [54] LEDC and Li_2CO_3 are not effectively protecting SEI components in long-term cycling experiments and also not at elevated temperatures, resulting in a continuous SEI growth.

Further influence from additives can be attributed to the

consumption of SN at 45 °C. Kim et al. [55] showed that SN improves the thermal stability of cathodes by suppressing thermally induced side reactions between $LiCoO_2$ (LCO) cathode and electrolyte. Moreover, better cycling performance was presented for NCM and LCO based cells at voltages up to 4.5 V [41] and for $LiNi_{0.5}Mn_{1.5}O_4$ (LNMO) based cells up to 5.2 V vs. Li/Li^+ [56] due to suppression of the electrolyte oxidation with the addition of SN.

Two electrolyte samples were extracted from cells aged at 20 °C and analyzed; one after 100 cycles representing the end of the
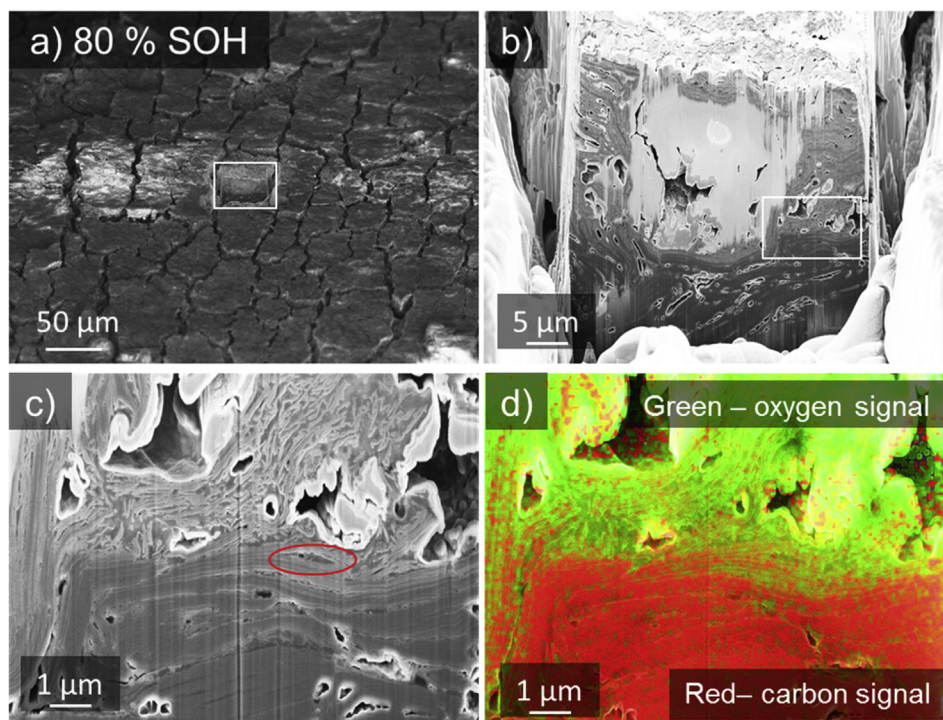
Fig. 6. SEM images of FIB prepared cross section of an aged anode (80% SOH, 20 °C, 1 C) at different magnifications (a–c). White frame indicates the magnified section. In d) EDX mapping results are shown for the cross section with oxygen and carbon signals marked in green and red, respectively. (For interpretation of the references to colour in this figure legend, the reader is referred to the web version of this article.)
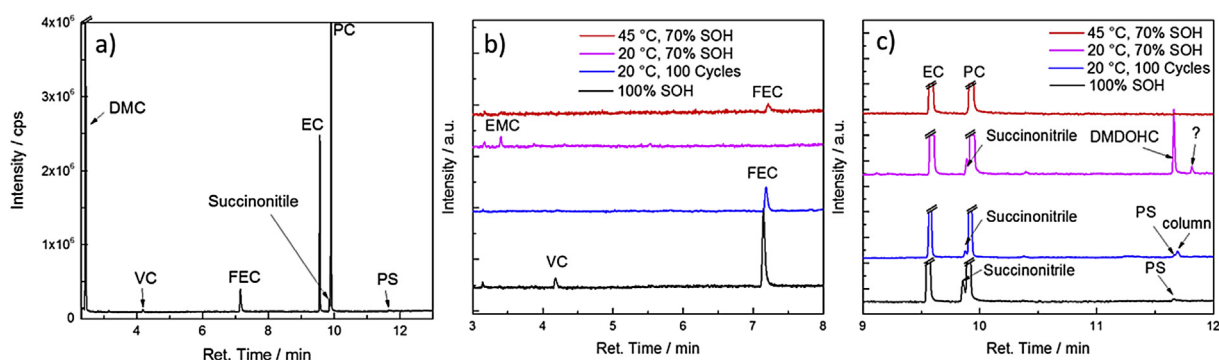

Fig. 7. GC-MS investigations: extracted electrolyte of a fresh cell (a) and comparisons of fresh and aged electrolytes at specific retention times in (b) and (c).

second aging section (Fig. 2) and at an SOH of 70% representing the cells EOL. FEC and PS are still present in the electrolyte after 100 cycles. Considering that FEC and PS are reduced on fresh graphite surfaces, this finding indicates a slow SEI growth process in this aging section, yet a change in the composition of the SEI can be assumed, as both components are continuously consumed with further cycling. As far as FEC is present in the electrolyte, an SEI is formed containing a large fraction of inorganic components. A further influence on the SEI composition as proposed by Xiang et al. [57] depends on the temperature. They demonstrate that more inorganic SEI components are formed at higher temperatures in a PC based electrolyte, suppressing graphite exfoliation [57]. Cycling at lower temperatures results in more organic components of the SEI, facilitating exfoliation [57]. In our case the electrolyte contains FEC. Thus, as long as FEC is still available, a high amount of inorganic SEI components will be formed and exfoliation will be suppressed to a great extent. In turn this means that after FEC has been consumed, the amount of organic SEI components will increase and

PC can co-intercalate, thus, leading to a thick layer with poor conductivity as obtained from the SEM and impedance results. The exfoliation is not observed at 45 °C, as increased PC and FEC reduction at higher temperature results in a more inorganic SEI composition.

An additional indicator for the modification of a effective to less effective SEI in the cells cycled at 20 °C is the observed increase of the electrolyte aging products dimethyl-2.5-dioxahexane carboxylate (DMDOHC), ethyl methyl carbonate (EMC) and an unknown decomposition product (marked in Fig. 7c), which is under further investigation. The formation of aging products correlates directly with the properties of the SEI [58,59]. Electrolyte decomposition and SEI is likely further enhanced, as it depends on the graphite surface area, which is enlarged after exfoliation [60,61].

3.5. Influence of the SEI on cyclic aging

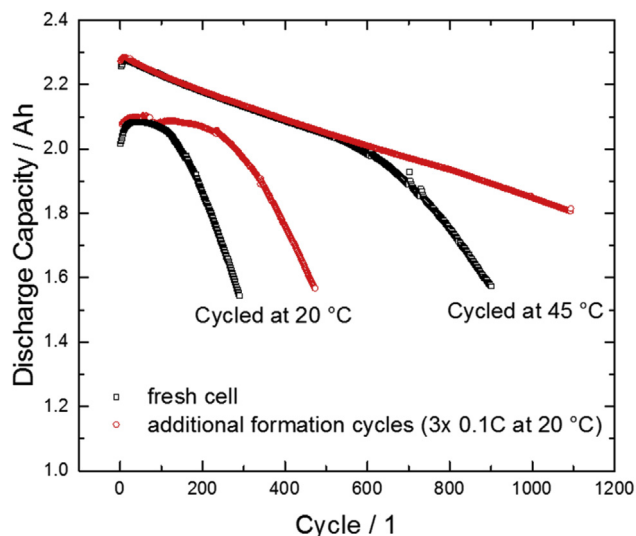To analyze the influence from the SEI on the cycling behavior,

Fig. 8. Cyclic aging of fresh cells compared to cells with additional formation cycles prior to further cyclic aging. The additional formation procedure consists of three cycles in the full voltage window with 0.1 C at 20 °C.

additional formation steps were performed on fresh cells. The formation procedure consists of 3 cycles with 0.1 C in the full voltage window at 20 °C, followed by cycling at the same cycling conditions as before. A comparison of cells cycled after additional formation and cells cycled as received from the manufacturer is shown in Fig. 8. At both temperatures cells with additional formation show an improved electrochemical performance. At 20 °C the undesired exfoliation phenomenon was delayed for more than 100 cycles. However, the overall fading behavior remains unchanged. The cell cycled at 45 °C shows in the beginning similar behavior. With advanced cycling the capacity fading rate stays linear, showing a better long-term cycling behavior compared to the cell without additional formation steps. The additional formation procedure enhances at both temperatures the cycling behavior and confirms the hypothesis of an ineffective SEI of the cells after formation at the manufacturer. As a result, the formation procedure of the cell producer is aiming rather at cost efficiency than at SEI quality and performance.

4. Conclusion

A comprehensive study of the effect of different aging temperatures, 20 °C and 45 °C, on lithium ion cells based a $Li(Ni_{0.5}Co_{0.2}Mn_{0.3})O_2$/graphite chemistry is presented in this paper. This study reveals the high complexity of interactions prevalent during aging. Even small changes, as the temperature in this case, can result in a propagation of electrochemical reactions leading to premature capacity fading or even safety issues. Herein it was possible to show a severe difference in the cell performance depending on the electrolyte composition, the interactions with the graphitic anode material and the applied temperature.

Moreover, the study shows the challenges of cell producers to develop cells for a wide temperature and application range. It shows the need for comprehensive studies combining electrochemical and *post-mortem* methods of the employed cell components, revealing the correlation of different aging mechanisms on the cell performance. Understanding the cell system is a key component for future applications, especially with growing cell sizes and battery packs in the field of electric vehicles and stationary storage systems. Furthermore, understanding the aging behavior of lithium ion cells is absolutely necessary to enable safe

and predictable second life applications of LIB.

In the second part of this study we focus on a correlation between aging and thermal stability of the herein examined cell types [62].

Appendix A. Supplementary data

Supplementary data related to this article can be found at http://dx.doi.org/10.1016/j.jpowsour.2016.12.040.

References

[1] P. Meister, H. Jia, J. Li, R. Kloepsch, M. Winter, T. Placke, Chem. Mater. 28 (2016) 7203—7217.
[2] H. Jia, R. Kloepsch, X. He, M. Evertz, S. Nowak, J. Li, M. Winter, T. Placke, Acta Chim. Slov. 63 (2016) 470—483.
[3] P. Bieker, M. Winter, Chem. Unserer Zeit 50 (2016) 172—186.
[4] D. Liu, J. Pang, J. Zhou, Y. Peng, M. Pecht, Microelectron. Reliab 53 (2013) 832—839.
[5] K. Asakura, M. Shimomura, T. Shodai, J. Power Sources 119—121 (2003) 902—905.
[6] J. Vetter, P. Novák, M.R. Wagner, C. Veit, K.-C. Möller, J.O. Besenhard, M. Winter, M. Wohlfahrt-Mehrens, C. Vogler, A. Hammouche, J. Power Sources 147 (2005) 269—281.
[7] V. Kraft, M. Grützke, W. Weber, J. Menzel, S. Wiemers-Meyer, M. Winter, S. Nowak, J. Chromatogr. A 1409 (2015) 201—209.
[8] M. Grützke, X. Mönnighoff, F. Horsthemke, V. Kraft, M. Winter, S. Nowak, RSC Adv. 5 (2015) 43209—43217.
[9] M. Börner, S. Klamor, B. Hoffmann, M. Schroeder, S. Nowak, A. Würsig, M. Winter, F.M. Schappacher, J. Electrochem. Soc. 163 (2016) A831—A837.
[10] S.-K. Jung, H. Gwon, J. Hong, K.-Y. Park, D.-H. Seo, H. Kim, J. Hyun, W. Yang, K. Kang, Adv. Energy Mater 4 (2014) 1300787.
[11] G. Gachot, S. Grugeon, G.G. Eshetu, D. Mathiron, P. Ribière, M. Armand, S. Laruelle, Electrochim. Acta 83 (2012) 402—409.
[12] S. Krueger, R. Kloepsch, J. Li, S. Nowak, S. Passerini, M. Winter, J. Electrochem. Soc. 160 (2013) A542—A548.
[13] J. Kasnatscheew, M. Evertz, B. Streipert, R. Wagner, R. Klöpsch, B. Vortmann, H. Hahn, S. Nowak, M. Amereller, A.-C. Gentschev, P. Lamp, M. Winter, Phys. Chem. Chem. Phys. 18 (2016) 3956—3965.
[14] D.R. Gallus, R. Wagner, S. Wiemers-Meyer, M. Winter, I. Cekic-Laskovic, Electrochim. Acta 184 (2015) 410—416.
[15] W. Weber, R. Wagner, B. Streipert, V. Kraft, M. Winter, S. Nowak, J. Power Sources 306 (2016) 193—199.
[16] M. Winter, Z. Phys. Chem. 223 (2009) 1395—1406.
[17] E. Peled, J. Electrochem. Soc. 126 (1979) 2047.
[18] G.-C. Chung, H.-J. Kim, S.-I. Yu, S.-H. Jun, J.-w. Choi, M.-H. Kim, J. Electrochem. Soc. 147 (2000) 4391.
[19] M. Klett, P. Svens, C. Tengstedt, A. Seyeux, J. Światowska, G. Lindbergh, R. Wreland Lindström, J. Phys. Chem. C 119 (2015) 90—100.
[20] R. Wagner, B. Streipert, V. Kraft, A. Reyes Jiménez, S. Röser, J. Kasnatscheew, D.R. Gallus, M. Börner, C. Mayer, H.F. Arlinghaus, M. Korth, M. Amereller, I. Cekic-Laskovic, M. Winter, Adv. Mat. Interfaces 3 (2016) 1600096.
[21] A. Friesen, F. Horsthemke, X. Mönnighoff, G. Brunklaus, R. Krafft, M. Börner, T. Risthaus, M. Winter, F.M. Schappacher, J. Power Sources 334 (2016) 1—11.
[22] M. Fleischhammer, T. Waldmann, G. Bisle, B.-I. Hogg, M. Wohlfahrt-Mehrens, J. Power Sources 274 (2015) 432—439.
[23] A. Friesen, C. Schultz, G. Brunklaus, U. Rodehorst, A. Wilken, J. Haetge, M. Winter, F. Schappacher, ECS Trans. 69 (2015) 89—99.
[24] D. Aurbach, B. Markovsky, A. Rodkin, M. Cojocaru, E. Levi, H.-J. Kim, Electrochim. Acta 47 (2002) 1899—1911.
[25] H. Schranzhofer, J. Bugajski, H.J. Santner, C. Korepp, K.-C. Möller, J.O. Besenhard, M. Winter, W. Sitte, J. Power Sources 153 (2006) 391—395.
[26] X. Qi, L. Tao, H. Hahn, C. Schultz, D.R. Gallus, X. Cao, S. Nowak, S. Röser, J. Li, I. Cekic-Laskovic, B.R. Rad, M. Winter, RSC Adv. 6 (2016) 38342—38349.
[27] S. Klamor, M. Schroder, G. Brunklaus, P. Niehoff, F. Berkemeier, F.M. Schappacher, M. Winter, Phys. Chem. Chem. Phys. 17 (2015) 5632—5641.
[28] H.-G. Schweiger, O. Obeidi, O. Komesker, A. Raschke, M. Schiemann, C. Zehner, M. Gehnen, M. Keller, P. Birke, Sensors 10 (2010) 5604—5625.
[29] A. Jossen, J. Power Sources 154 (2006) 530—538.
[30] M.D. Levi, D. Aurbach, J. Phys. Chem. B 101 (1997) 4630—4640.
[31] T. Yoon, S. Park, J. Mun, J.H. Ryu, W. Choi, Y.-S. Kang, J.-H. Park, S.M. Oh, J. Power Sources 215 (2012) 312—316.
[32] H. Buqa, M. Holzapfel, F. Krumeich, C. Veit, P. Novák, J. Power Sources 161 (2006) 617—622.
[33] M. Winter, J.O. Besenhard, M.E. Spahr, P. Novák, Adv. Mater 10 (1998)

725–763.

[34] M.R. Wagner, P.R. Raimann, A. Trifonova, K.-C. Möller, J.O. Besenhard, M. Winter, Anal. Bioanal. Chem. 379 (2004) 272–276.

[35] J.O. Besenhard, M. Winter, J. Yang, W. Biberacher, J. Power Sources 54 (1995) 228–231.

[36] M.R. Wagner, J.H. Albering, K.-C. Moeller, J.O. Besenhard, M. Winter, Electrochem. Commun. 7 (2005) 947–952.

[37] M. Winter, G.H. Wrodnigg, J.O. Besenhard, W. Biberacher, P. Novák, J. Electrochem. Soc. 147 (2000) 2427.

[38] M. Winter, W.K. Appel, B. Evers, T. Hodal, K.-C. Möller, I. Schneider, M. Wachtler, M.R. Wagner, G.H. Wrodnigg, J.O. Besenhard, Monatsh. Chem. 132 (2001) 473–486.

[39] K. Tasaki, A. Goldberg, M. Winter, Electrochim. Acta 56 (2011) 10424–10435.

[40] J. Kasnatscheew, R.W. Schmitz, R. Wagner, M. Winter, R. Schmitz, J. Electrochem. Soc. 160 (2013) A1369–A1374.

[41] G.-Y. Kim, J.R. Dahn, J. Electrochem. Soc. 162 (2014) A437–A447.

[42] H. Ota, K. Shima, M. Ue, J.-i Yamaki, Electrochim. Acta 49 (2004) 565–572.

[43] B. Zhang, M. Metzger, S. Solchenbach, M. Payne, S. Meini, H.A. Gasteiger, A. Garsuch, B.L. Lucht, J. Phys. Chem. C 119 (2015) 11337–11348.

[44] S.S. Zhang, J. Power Sources 162 (2006) 1379–1394.

[45] R. McMillan, H. Slegr, Z. Shu, W. Wang, J. Power Sources 81–82 (1999) 20–26.

[46] R. Mogi, M. Inaba, S.-K. Jeong, Y. Iriyama, T. Abe, Z. Ogumi, J. Electrochem. Soc. 149 (2002) A1578.

[47] M.-H. Ryou, G.-B. Han, Y.M. Lee, J.-N. Lee, D.J. Lee, Y.O. Yoon, J.-K. Park, Electrochim. Acta 55 (2010) 2073–2077.

[48] H. Nakai, T. Kubota, A. Kita, A. Kawashima, J. Electrochem. Soc. 158 (2011) A798.

[49] Y.-M. Lin, K.C. Klavetter, P.R. Abel, N.C. Davy, J.L. Snider, A. Heller, C.B. Mullins, Chem. Commun. 48 (2012) 7268.

[50] M. Matsumoto, T. Sanada, N. Takao, M. Mogi, T. Matsuda, K. Ando, D. Imamura, H. Imai, ECS Trans. 69 (2015) 13–25.

[51] D. Aurbach, K. Gamolsky, B. Markovsky, Y. Gofer, M. Schmidt, U. Heider, Electrochim. Acta 47 (2002) 1423–1439.

[52] X. Zuo, M. Xu, W. Li, D. Su, J. Liu, Electrochem. Solid-State Lett. 9 (2006) A196.

[53] M. Xu, W. Li, B.L. Lucht, J. Power Sources 193 (2009) 804–809.

[54] M. Herstedt, D.P. Abraham, J.B. Kerr, K. Edström, Electrochim. Acta 49 (2004) 5097–5110.

[55] Y.-S. Kim, H. Lee, H.-K. Song, ACS Appl. Mat. Interfaces 6 (2014) 8913–8920.

[56] R. Chen, F. Liu, Y. Chen, Y. Ye, Y. Huang, F. Wu, L. Li, J. Power Sources 306 (2016) 70–77.

[57] H.F. Xiang, C.H. Chen, J. Zhang, K. Amine, J. Power Sources 195 (2010) 604–609.

[58] G. Gachot, P. Ribière, D. Mathiron, S. Grugeon, M. Armand, J.-B. Leriche, S. Pilard, S. Laruelle, Anal. Chem. 83 (2011) 478–485.

[59] M. Grützke, V. Kraft, W. Weber, C. Wendt, A. Friesen, S. Klamor, M. Winter, S. Nowak, J. Supercrit. Fluids 94 (2014) 216–222.

[60] M. Winter, J. Electrochem. Soc. 145 (1998) 428–436.

[61] J.P. Olivier, M. Winter, J. Power Sources 97–98 (2001) 151–155.

[62] M. Börner, A. Friesen, M. Grützke, Y.P. Stenzel, G. Brunklaus, J. Haetge, S. Nowak, F.M. Schappacher, M. Winter, J. Power Source XY (2017) pp-pp. http://dx.doi.org/10.1016/j.jpowsour.2016.12.041 (published in parallel with this paper).